



This is a repository copy of *Thermal near infrared monitoring system for electron beam melting with emissivity tracking*.

White Rose Research Online URL for this paper:
<http://eprints.whiterose.ac.uk/132138/>

Version: Published Version

Article:

Boone, N.A. orcid.org/0000-0002-5251-0104, Zhu, C., Smith, C. et al. (2 more authors) (2018) Thermal near infrared monitoring system for electron beam melting with emissivity tracking. *Additive Manufacturing*, 22. pp. 601-605. ISSN 2214-8604

<https://doi.org/10.1016/j.addma.2018.06.004>

© 2018 The Authors. Published by Elsevier B.V. This is an open access article under the CC BY license (<http://creativecommons.org/licenses/by/4.0/>).

Reuse

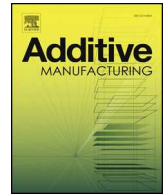
This article is distributed under the terms of the Creative Commons Attribution (CC BY) licence. This licence allows you to distribute, remix, tweak, and build upon the work, even commercially, as long as you credit the authors for the original work. More information and the full terms of the licence here:
<https://creativecommons.org/licenses/>

Takedown

If you consider content in White Rose Research Online to be in breach of UK law, please notify us by emailing eprints@whiterose.ac.uk including the URL of the record and the reason for the withdrawal request.



eprints@whiterose.ac.uk
<https://eprints.whiterose.ac.uk/>



Full length article

Thermal near infrared monitoring system for electron beam melting with emissivity tracking

N. Boone^a, C. Zhu^a, C. Smith^b, I. Todd^b, J.R. Willmott^{a,*}^a Department of Electronic & Electrical Engineering, University of Sheffield, UK^b Department Materials Science, University of Sheffield, UK

ARTICLE INFO

Keywords:

Thermal imaging
Electron beam melting
Process monitoring

ABSTRACT

This paper presents the design of a high speed, high resolution silicon based thermal imaging instrument and its application to thermally image the temperature distributions of an electron beam melting additive manufacturing system. Typically, thermal images are produced at mid or long wavelengths of infrared radiation. Using the shorter wavelengths that silicon focal plane arrays are sensitive to allows the use of standard windows in the optical path. It also affords fewer modifications to the machine and enables us to make use of mature silicon camera technology. With this new instrument, in situ thermal imaging of the entire build area has been made possible at high speed, allowing defect detection and melt pool tracking. Melt pool tracking was used to implement an emissivity correction algorithm, which produced more accurate temperatures of the melted areas of the layer.

1. Introduction

Additive Manufacturing (AM) is a rapidly developing, yet comparatively immature manufacturing technology [1]. AM parts are created directly from precise Computer Aided Design (CAD) models and currently suffer from dimensional variations, rough surface finishes, and internal defects not present in those models. These issues present a barrier for uptake amongst the advanced manufacturing sectors most likely to benefit from the design freedom AM brings; for example, aerospace and automotive. One potential solution to these issues is advancement of in-process monitoring systems. AM processes typically rely upon heat to fuse particles of deposited materials. Thermal imaging is, therefore, ideal for AM in-process monitoring. Progress so far in this field has concentrated on the use of mid and long wavelength infrared (IR) imaging technologies [2,3].

Common thermal imaging products and systems use focal-plane-array (FPA) technologies that include InSb detectors [3] and microbolometers [2]. These are sensitive to mid-wavelength IR (MWIR) (3–5 μm) and long-wavelength IR (LWIR) (7.5–14 μm), respectively. Typical, high-end thermal cameras produce images with VGA resolution (640 \times 480) and frame rates of 9–15 Hz. Silicon FPAs are sensitive to visible wavelengths of optical radiation and are ubiquitous in consumer imaging products. Although silicon FPAs are usually optimised for visible wavelength sensitivity (400–700 nm), their responsivity spectrum has significant sensitivity in the near infrared (NIR), which

typically extends across 750–1050 nm. The maturity of silicon as an optical radiation sensitive material and the huge volume of silicon FPAs that have been developed, has led to silicon out performing other FPA technologies. For example, it is common to find multi-megapixel silicon detectors that produce fast (> 60 Hz) or ultra-fast (> 1000 Hz) frame rates.

AM is a demanding application for thermal imaging; particularly Electron Beam Melting (EBM). Imaging must not only be sufficiently high resolution to show the formation of variations from CAD models, it must also be sufficiently high speed to capture the time-resolved interaction of the electron beam with metal powder. We, therefore, decided to use mature silicon technology for our AM thermal imaging.

Our AM system is of the EBM type and was developed by Arcam [4]. The process in the Arcam A2 is similar to other metal AM processes, specifically powder bed fusion (PBF); where a 3D object is built layer by layer, using an electron beam as the input energy source. The use of an electron beam, in preference to a laser, allows the beam to be steered across the build area at a very high speed, using electromagnetic deflection coils (Fig. 1). This contrasts with the slower mechanical parts found in other approaches to AM and dictates a higher speed monitoring solution is needed for effective use of this technology. The use of an electron beam necessitates the process to operate under vacuum and with elevated bed temperatures to sinter the powder before melting. These requirements have advantages in reducing the chamber oxygen content and residual stresses in the parts when compared with standard

* Corresponding author.

E-mail address: j.r.willmott@sheffield.ac.uk (J.R. Willmott).<https://doi.org/10.1016/j.addma.2018.06.004>

Received 22 March 2018; Received in revised form 7 June 2018; Accepted 10 June 2018

Available online 15 June 2018

2214-8604/ © 2018 The Authors. Published by Elsevier B.V. This is an open access article under the CC BY license (<http://creativecommons.org/licenses/by/4.0/>).

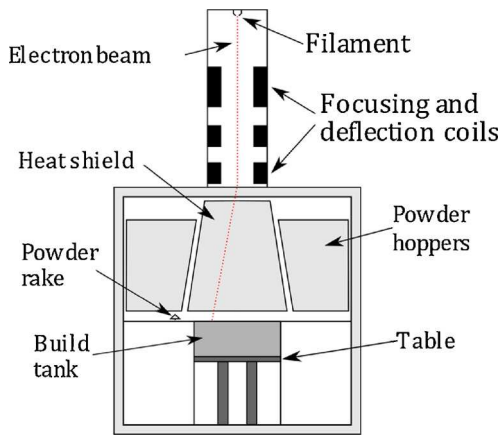


Fig. 1. Arcam A2 EBM system diagram.

laser processes [5]. The vacuum itself does not pose any problem for thermal imaging, however, the system design had to take this into account by ensuring any parts mounted to the vacuum chamber made an adequate seal. The elevated bed temperature is much lower than the temperature at which the powder melts (1003 K vs 1933 K for Ti-6Al-4V) and so the cooling rates are significant; hence the instrument measurement range must cover a very wide temperature range. The current state of in-process monitoring for AM is limited, especially for the EBM process. Most of the work on comprehensive monitoring systems is at the research stage [2,3], with only Arcam’s LayerQam [6] technology available commercially.

2. Materials and methods

2.1. Instrument design

The thermal imaging instrument comprised a Hamamatsu C11440-22CU silicon sCMOS camera [7], sensitive to wavelengths from 400 nm to 1 μm and with a resolution of 2048 × 2048 pixels. A custom designed ‘borescope’ lens system was produced, together with a redesigned vacuum chamber mount and Kapton film feed system. This provided an alignment mechanism for the borescope and prevented metallisation of the window behind which the borescope is mounted. The borescope lens design allowed the camera to be mounted away from the vacuum chamber (Fig. 2). This gave easy access for imaging with minimal modification to the Arcam A2. Significant modifications were not recommended due to the risk of X-Ray radiation generated within the process. A consequence of this was the need to use lead glass in the optical system. Imaging in the NIR allowed us to do this because the transmission of the glass at this wavelength range is > 90% (reducing to 76% when combined with the Kapton film), compared to 1.08% found by R. B. Dinwiddie et. al [3]. when imaging in the MWIR.

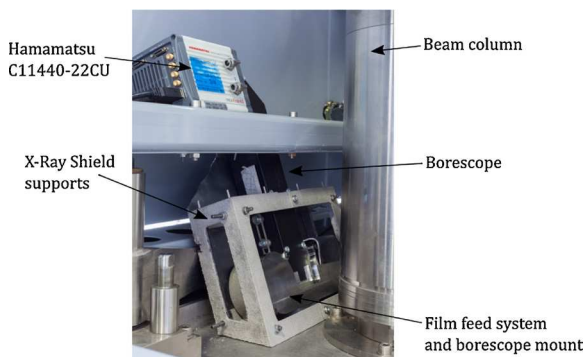


Fig. 2. Full instrument mounted on Arcam A2.

Therefore, the camera could be used at its full potential with low exposure times and high framerates. It also allowed imaging through all phases of the build, unlike E. Rodriguez et. al [2]. where a shutter was used to prevent metallisation and therefore images could only be acquired when the process was not in the melting phase. Using a shorter wavelength camera also decreased the effect of emissivity on the measurements [8,9] compared to the longer wavelength technologies; resulting in a lower measurement uncertainty. This can be shown by calculating the percentage signal (DL) change per K change in temperature [10] using:

$$\% / K = 100 \times \frac{c_2}{\lambda T^2}$$

where c_2 is Planks second radiation constant 1.4388×10^{-2} m. K, T is the blackbody temperature in Kelvin and λ is the mean effective wavelength of the FPA. The %/K for typical infrared detectors are tabulated below for the standard preheat temperature of 1003 K. These calculations show that a small change in emissivity of, for example, 0.01 (1% of signal) will have a much greater effect on the measured temperature for the longer the wavelength detectors.

Wavelength (μm)	% Change in Signal per K	Error in K from emissivity incorrect by 0.01
1 (Silicon NIR)	1.43	0.70
4 (InSb MWIR)	0.36	2.78
10.75 (Microbolometer LWIR)	0.13	7.70

The vacuum chamber viewing port on the A2 was not located directly above the build plate, due to the position of the beam column, which resulted in the camera and lens being angled at approximately 20° from the build plate normal (Fig. 2). This allowed the entire build plate to be visible in-frame, with the focal point located at the centre of the build plate, at 400 mm working distance. The pixel radius on the imaging plane at the centre field of view was 66 μm, increasing to 79 μm at the maximum distance from the centre. The borescope design consisted of eleven lenses and a mirror, four of the lenses were custom designed (Fig. 3), with the remainder acquired from a catalogue supplier. The borescope had an f/# of 6 and a field of view covering 230 mm in diameter. The design consisted of an outer housing which held the lenses, with the lenses separated by sections of lens tube according to the spacing required by the design. The assembled borescope is shown in Fig. 4. A bandpass filter was fitted to the back of the borescope to define the wavelength range of the camera and to eliminate the majority of visible wavelengths (daylight) from reaching the FPA.

Filter selection was crucial to obtaining the temperature range and resolution required of the instrument. The planned temperature range for imaging with the instrument spanned from the standard preheat temperature of approximately 1003 K to the melting point of the

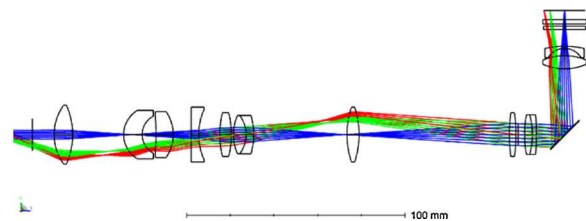


Fig. 3. Borescope lens design showing paths through the optical system (from the object plane on the left to image plane at the top) for on axis rays (blue), the maximum field of view (red) and 1/√2 field of view (green) (For interpretation of the references to colour in this figure legend, the reader is referred to the web version of this article).

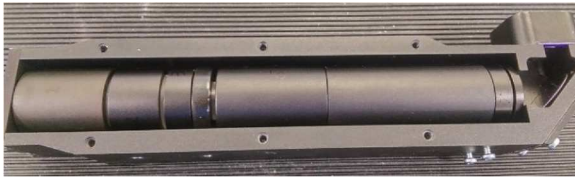


Fig. 4. Assembled borescope, with side panel removed, showing lens mounting system.

Titanium alloy (Ti-6Al-4 V) at 1933 K. The non-linear nature of Planck’s law dictated that there was a reduction in resolvable temperature difference at lower temperatures [8]. When imaging at high resolution and lower temperatures, the exposure time setting in the camera could be increased to move the measurement temperature range to a lower minimum value. An 850 nm long pass filter was evaluated to maximise transmission in the NIR band; with consideration of the silicon FPA’s relatively low quantum efficiency (QE), of 35% at 850 nm, which reduced to less than 10% at 1 μ m.

Uncertainty in the measurement was increased by the Arcam A2 environment. Surrounding the build plate was a series of heat shields (Fig. 1) designed to reflect radiated heat back into the confined build area. It seemed likely that these would be a cause of stray radiation in the enclosed environment. After initial testing with the camera mounted in front of a blackbody furnace, and subsequently in situ mounted in the machine, a much higher signal was found than expected. A maximum range of 799 K–1272 K was measurable with our instrument assembled as described. A neutral density (ND) filter with optical density (OD) of 2 was added to the optical system (Thorlabs, NENIR20B) which adjusted the maximum range to 875 K–1581 K. This was much closer to the range originally required of the instrument. The discrepancy was most likely a result of our lack of knowledge of the QE of the FPA, which was quoted with reliable data to only 1 μ m by the manufacturer. In combination with the 850 nm long pass filter, our system had an optical bandwidth of at least 150 nm, with the aforementioned imprecisely defined long wavelength edge.

Planck’s law [8] was used to model the signal levels when using the 850 nm long pass filter with OD 2 ND filter and later, for evaluating several other filters. This was accomplished by integrating Planck’s law over the approximate wavelength range defined by the combination of filter transmission and silicon FPA responsivity spectrum (850 nm – 1 μ m). Resulting curves were scaled to conform to the digital levels (DLs) of signal output by the camera. This process was repeated with the characteristics of candidate filters, with narrow bandwidths and centre wavelengths in the wavelength range of the camera responsivity spectrum (Fig. 5). In this way, the trade off in the QE of the silicon FPA at longer wavelengths was evaluated as a function of distance from the peak wavelength of the temperature range of the system as defined by Wien’s law [11].

A 990 nm bandpass filter was found to provide the optimum

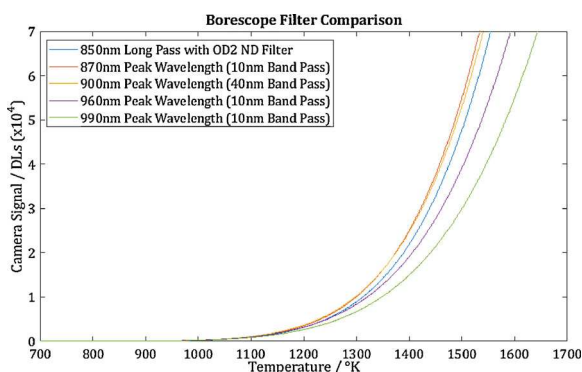


Fig. 5. Borescope filter comparison.

temperature range required to thermally image the titanium powder EBM process. The temperature measurement range was 950 K–1630 K. Further characterisation and calibration of the system was achieved using this setup, producing a more accurately modelled range and signal to temperature conversion.

2.2. Melt pool tracking

Melt pool tracking was enabled by the high-speed capability of the camera and would be considerably less effective with lower frame rate systems; due to the speed at which the melt pool moves around the image. The melt pool was identified in each image using blob detection techniques [12] in post processing, using approximate melt pool area (60px) and diameter (10px) as well as average DL(28,500) to assist the algorithm in detection. This is more accurate, when compared to a simple thresholding technique and allowed individual tracking of multiple simultaneous melt pools. A mask of pixels that the melt pool covered from the start of the layer was created by detecting the melt pool in each image individually, then combining the detected areas of all previous images. This mask now contains the previously melted area and is created for each image in the sequence. The emissivity correction then used the melt-pool-tracking mask to apply an emissivity value to each pixel, based on whether it had been classified as melted or unmelted. Accurate measurement of temperature is only possible if the emissivity of the measured body is known and accounted for. Emissivity may change as a function of temperature and it would be expected that the change be greatest following a phase transition.

2.3. Monitoring an EBM build

The instrument was used in situ to investigate thermal properties during the entirety of several AM builds and with Arcam’s Ti-6Al-4 V titanium alloy powder. Images from the melting and cooling phases of each layer were used to look for differences in radiance temperature [8] of the melted part surface. The ability to image throughout the melting phase allowed the melt pool to be tracked and our system to more accurately correct for emissivity. Our hypothesis was based on the precept that emissivity will change significantly between liquid and solid phases and otherwise can be considered to remain constant.

A sample with four different overhanging features (two ledge overhangs of different thicknesses and two sloped overhangs) was designed to probe the process (see Fig. 6). Overhangs (or negative surfaces) present a challenge for powder bed processes because the thermal conductivity of the powder is much lower than that of prior melted material [13]. With the dissipation of heat being much slower, the use of support structures to aid heat removal in combination with a reduced beam energy input must be applied to maintain dimensional accuracy. Reducing the energy input too much, however, will produce defects, due to poor fusion which may promote the occurrence of

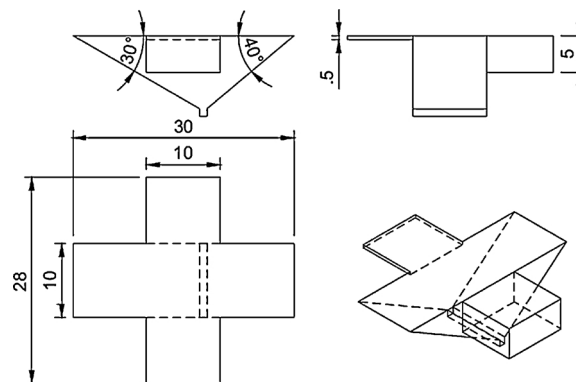


Fig. 6. Overhang sample part (dimensions in mm).

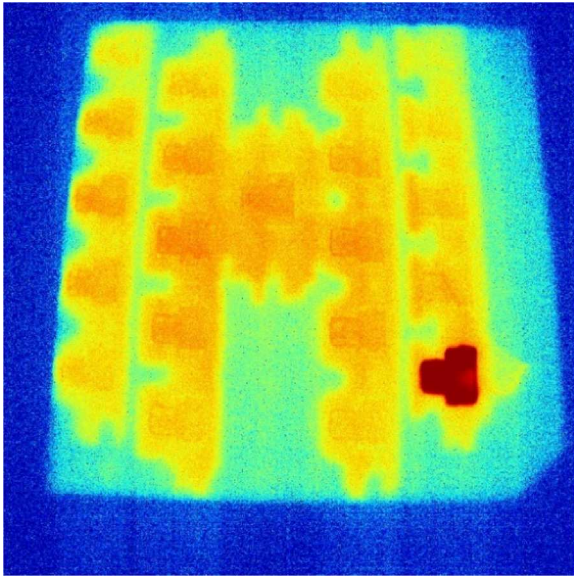


Fig. 7. 'T' Shaped test pieces showing the effect of residual heat from the previous layer.

chimney defects [14]. Overhangs thus present a suitable opportunity for in-situ monitoring of defects. The samples were produced with Arcam standard preheat and melt themes for 70 μm layers included with EBM control V3.2.121.

3. Results

The thermal image in Fig. 7 was captured early in the melting phase. The parts in this image are small (25 x 25 mm) 'T' shaped parts, aligned in five columns on the bed. In the time between the end of the melting phase of the previous layer and the start of preheat for the next layer, the table was lowered, and a new layer of powder was deposited. The now current top layer was lightly sintered in the preheat phase and the outline of each part was melted in the contour phase. The thermal transfer from the melted parts of the previous layer and the contour can be seen on the image as enlarged outlines. The previous layer contributed additional radiance because the contour had a relatively low power input into the bed, compared to the residual heat from the previous layer. This thermal transfer between layers is essential to the process, assisting with layer adhesion and powder bed sinter density leading to better melt pool definition [15] and also effecting material properties such as porosity and microstructure [16]. The spatial resolution in Fig. 7 is lower than the usual high performance of our instrument because the image contrast has been adjusted to a narrow temperature range to clearly show this effect of thermal transfer between layers, making the image appear noisy.

The thermal image in Fig. 8 is from an evaluation of support structures, used to support overhanging faces and sink heat away from the overhanging layers [17]. This image shows evidence of both swelling and lack of fusion defects on the cross shaped pieces, for geometry see Fig. 6. The image was captured whilst the two parts shown were cooling. The left-hand part cooled for a longer period of time compared to the other part. Each part had an optimised melt strategy with the intension of minimising swelling. The swelling, indicated in the figure as the darker red section above the arrow, is evidence of excess power being input into a volume of material in relation to the potential of the structure to 'sink' the heat away. The resulting part geometry deformation can be seen in the built part photographed in Fig. 9.

Evidence of lack of fusion defects can be seen on the bottom section of both parts in Fig. 8; manifesting as the apparent hot spots. These are either closed or buried within the parts and so cannot be seen in Fig. 9.

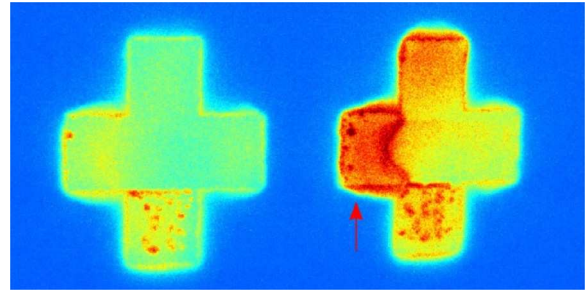


Fig. 8. Cross pieces showing lack of fusion defects (small localised apparent hot spots) and swelling (indicated with marker) (see Appendix A Visualisation 1 for video).



Fig. 9. Physical cross pieces showing evidence of swelling (indicated with marker).

The small cavity filled with unmelted powder likely creates a small blackbody cavity, causing the apparent increase in temperature compared to the rest of the melted layer; when in fact it is only an increase in emissivity.

Both of these defects could be corrected for if detected in real time during a build, either by lowering energy input into areas of swelling or increasing it in unmelted areas.

Emissivity corrected imaging was accomplished using the melt pool tracking technique described above. Fig. 10 shows a part thermally imaged with and without emissivity tracking. Image A shows the image with no emissivity correction, B shows the mask that has been constructed by tracking the melt pool on previous images and C shows the image corrected for emissivity differences between melted and unmelted powder. Melted powder is hotter than unmelted powder, yet there is very little contrast in the thermal image in Fig. 10A. The emissivity of liquid metal is likely to be lower than for the corresponding material solid phase where rough surfaces are present [18]. Reduction in emissivity is concomitant with a reduction in radiance in an isothermal system [8]. The lower emissivity of the liquid metal led to a greater reduction in radiance temperature, from that of a blackbody, compared to the solid powder. Therefore, Fig. 10A appears to be low in contrast because the radiance temperature of the liquid metal is disproportionately lower than for the solid powder, yet the temperature of the liquid is higher. The result is that an uncorrected image will have low contrast. Once the emissivity differences have been accounted for and corrected in Fig. 10C, the image shows markedly increased contrast in temperature. When comparing temperature values between the



Fig. 10. Images showing emissivity correction by melt pool tracking, temperature scale in K (A) no emissivity correction; (B) emissivity mask; (C) emissivity corrected image Apparent temperature at centre of marked X 1183 K (uncorrected image), 1275 K (corrected image).

images with and without emissivity correction, a temperature increase of around 90 K is seen within the corrected area in the corrected images.

4. Conclusion

In conclusion, this report has described the design and use of a silicon FPA based imaging system and articulated the advantages of this technology compared to other thermal imaging modalities. This system brings higher speed and spatial resolution over existing solutions, together with an accurate temperature calibration. There are several potential advantages to such an approach including: high resolution, high frame rate, using the relatively low-cost silicon FPA technology. This makes it ideal for in process monitoring of AM systems like EBM. Also described was the implementation of our melt pool tracking and our corollary process of emissivity correction, which is an important step towards accurate contactless temperature measurement in the EBM environment. It is anticipated that our system will allow accurate online detection of defects based on high speed image analysis in the future.

Acknowledgement

The authors would like to gratefully acknowledge the Engineering and Physical Sciences Research Council (EPSRC) for supporting the research with grant EP/M009106/1.

Appendix A. Supplementary data

Supplementary material related to this article can be found, in the online version, at doi:<https://doi.org/10.1016/j.addma.2018.06.004>.

References

- [1] Y. Huang, M.C. Leu, J. Mazumder, A. Donmez, Additive manufacturing: current State, future potential, gaps and needs, and recommendations, *J. Manuf. Sci. Eng.* 137 (2015) 014001, <http://dx.doi.org/10.1115/1.4028725>.
- [2] E. Rodriguez, F. Medina, D. Espalin, C. Terrazas, D. Muse, C. Henry, E. MacDonald, R.B. Wicker, Integration of a thermal imaging feedback control system in electron beam melting, 23rd Annu. Int. Solid Free. Fabr. Symp. Addit. Manuf. Conf. (2012), pp. 945–961 <https://sffsymposium.engr.utexas.edu/Manuscripts/2012/2012-72-Rodriguez.pdf>.
- [3] R.B. Dinwiddie, M.M. Kirka, P.D. Lloyd, R.R. Dehoff, L.E. Lowe, G.S. Marlow, Calibrating IR Cameras for in-Situ Temperature Measurement During the Electron Beam Melt Processing of Inconel 718 and Ti-Al6-V4, (2016), p. 986107, <http://dx.doi.org/10.1117/12.2229070>.
- [4] A.B. Arcam, Additive Manufacturing - Arcam AB, (N.D.) (Accessed December 19, 2017), <http://www.arcam.com/technology/additive-manufacturing/>.
- [5] P.K. Gokuldoss, S. Kolla, J. Eckert, Additive manufacturing processes: selective laser melting, electron beam melting and binder jetting-selection guidelines, *Mater.* (Basel). 10 (2017), <http://dx.doi.org/10.3390/ma10060672>.
- [6] A.B. Arcam, Process Validation Tools, (N.D.) (Accessed November 9, 2017), <http://www.arcam.com/technology/electron-beam-melting/process-validation-tools/>.
- [7] Hamamatsu, ORCA-flash4.0 v2, (n.d.) 1–8. https://www.hamamatsu.com/resources/pdf/sys/SCAS0081E_C11440-22CU.pdf (Accessed December 19, 2017).
- [8] P. Saunders, SPIE press, *Radiation Thermometry : Fundamentals and Applications in the Petrochemical Industry*, (2007).
- [9] J. Dixon, Radiation thermometry, *J. Phys. E.* 21 (1988) 425–436, <http://dx.doi.org/10.1088/0022-3735/21/5/001>.
- [10] J. Taylor, L. Instruments, FoundAtion Level Infrared Training, Land Instruments International Ltd, 2010, <https://www.isa.org/WorkArea/DownloadAsset.aspx?id=136908>.
- [11] British Standards Institute, BS 1041-5 Temperature Measurement Part 5: Guide to Selection and Use of Radiation Pyrometers, BSI, (1989) <https://bsol.bsigroup.com/Bibliographic/BibliographicInfoData/000000000000209496>.
- [12] R. Davies, Circle and ellipse detection, *Comput. Mach. Vis. Theory, Algorithms, Pract.* 4th ed., Elsevier, 2012, pp. 303–333, <http://dx.doi.org/10.1016/C2010-0-66926-4>.
- [13] C.J. Smith, S. Tammas-Williams, E. Hernandez-Nava, I. Todd, Tailoring the thermal conductivity of the powder bed in electron beam melting (EBM) additive manufacturing, *Sci. Rep.* 7 (2017), <http://dx.doi.org/10.1038/s41598-017-11243-8>.
- [14] C.J. Smith, F. Derguti, E. Hernandez Nava, M. Thomas, S. Tammas-Williams, S. Gulizia, D. Fraser, I. Todd, Dimensional accuracy of electron beam melting (EBM) additive manufacture with regard to weight optimized truss structures, *J. Mater. Process. Technol.* 229 (2016) 128–138, <http://dx.doi.org/10.1016/j.jmatprotec.2015.08.028>.
- [15] C. Körner, E. Attar, P. Heinel, Mesoscopic simulation of selective beam melting processes, *J. Mater. Process. Technol.* 211 (2011) 978–987, <http://dx.doi.org/10.1016/J.JMATPROTEC.2010.12.016>.
- [16] H. Galarraga, D.A. Lados, R.R. Dehoff, M.M. Kirka, P. Nandwana, Effects of the microstructure and porosity on properties of Ti-6Al-4V ELI alloy fabricated by electron beam melting (EBM), *Addit. Manuf.* 10 (2016) 47–57, <http://dx.doi.org/10.1016/J.ADDMA.2016.02.003>.
- [17] B. Vayre, F. Vignat, F. Villeneuve, Identification on some design key parameters for additive manufacturing: application on electron beam melting, *Procedia CIRP* (2013) 264–269, <http://dx.doi.org/10.1016/j.procir.2013.05.045>.
- [18] E. Belskaya, Emissivity and electrical resistivity of titanium alloys with aluminum and vanadium, *High. Temp.* 50 (2012) 475–478, <http://dx.doi.org/10.1134/S0018151X12040049>.